Investigations of skin friction drag mitigation over viscoelastic surfaces in supersonic flows

Soumen Chakravarty* and V. Narayanaswamy†
Department of Mechanical and Aerospace Engineering, North Carolina State University, Raleigh, North Carolina 27606, USA

(Received 15 June 2023; accepted 25 April 2024; published 22 May 2024)

Drag mitigation by passive surfaces with engineered material properties has gained significant attention in low-speed flows. The present work investigates the skin friction drag mitigation caused by flow interactions with a nonrigid surface at supersonic speeds. The nonrigid surface was formed by implanting viscoelastic rubber materials of different elastic moduli over a rigid surface. Direct measurements of the skin friction coefficient (C_f) were made along the length of the viscoelastic surfaces and compared against the corresponding values over a rigid surface. The C_f over the implants employed in this work demonstrated measurable decrease compared to a rigid surface along their entire length. A maximum local decrease in C_f of 30% was measured at a station located 30 mm downstream of the implant leading edge, demonstrating that the boundary layer responds to the presence of the compliant surface within a short distance after encountering the surface. The mechanisms that drive the reduction in C_f was investigated through a combination of turbulent statistics measurements and theoretical analysis. The results suggest that the unsteady deformations of the viscoelastic surface can affect VLSMs (very large-scale motions) as well as the near-wall burst cycles, which in turn could drive the observed C_f mitigation.

DOI: 10.1103/PhysRevFluids.9.054609

I. INTRODUCTION

Turbulent skin friction contributes to a major fraction of the total drag experienced by slender vehicles across all speed regimes and also results in elevated pressure head requirements and heating issues in internal flows. Efforts to mitigate skin friction drag has been undertaken over several decades and have been periodically documented in multiple texts (White [1] and Schlichting [2]). Corke [3] in his review broadly categorizes the different drag mitigation approaches as those that modify the near-wall turbulent streaks (e.g., riblets, vortex generators, plasma discharges, etc.) and those that affect the outer scales of the boundary layer (e.g., jet blowing, airfoils, etc., placed in the outer region of the boundary). While both these types of approaches have exhibited noticeable success with drag mitigation, direct modulation of the near-wall streaks possesses noticeable advantages owing to their ease of implementation in practical systems, opportunities to scale up geometrically, among others. As a result, significantly greater fraction of the literature addressed drag mitigation by near-wall turbulence modification. A select number of these approaches are reviewed here.

Riblets are among the most widely used drag mitigation devices. Optimized riblets have demonstrated drag reduction up to 10% in subsonic and transonic flows (Viswanath [4]). Choi [5] proposed that the riblets restrict the spanwise meandering of the near-wall streaks, which in turn weakens the

*Graduate Research Assistant
†Professor; vnaraya3@ncsu.edu

near-wall tubulent bursts, and reduces the wall shear stress. Interestingly, increasing the size of the riblets substantially beyond optimum caused an increase in the skin friction drag. Garcia-Mayoral and Jimenez [6] posit that the drag. increase for these large riblets is due to appearance of spanwise Kelvin Helmholtz type structures, which increases the Reynolds stress. Using DNS, Choi *et al.* [7] showed that optimally sized riblets also prevent the penetration of the downwash induced by streamwise vortices into the wall. Riblet-based drag mitigation have also been investigated in supersonic flows by Coustols and Cousteix [8], Gaudet [9], and Robinson [10]. A maximum drag reduction of 7% was obtained from all these efforts, which is remarkably similar to the optimal riblet performance in subsonic flows. Computations by Duan and Choudhari [11,12] agreed closely with the experimental findings and also showed that the drag reduction mechanisms and resulting flow features follow their low-speed counterparts.

Application of permeable walls for drag modification has also garnered significant interest since the early 2000s. Breugem [13] predicted a complete modification of near-wall turbulence in the presence of an isotropic permeable wall, with the near-wall turbulent streaks being replaced by spanwise Kelvin Helmholtz structures, creating higher Reynolds shear stress. Both Abderrahaman and Garcia-Mayoral [14] and Gomez De Segura *et al.* [15] showed that the appearance of the spanwise rollers is strongly dependent on the wall-normal permeability and increasing the streamwise permeability has a favorable effect on drag reduction. These studies led to the use of anisotropic surfaces for drag reduction. Kuwata and Suga [16] and Rosti *et al.* [17] numerically demonstrated that anisotropic surfaces indeed yield drag reduction. Of significant interest is the fact that the drag reduction did not saturate with increasing the streamwise permeability. The authors hypothesized that the drag reduction from the anisotropic surfaces was caused by the attenuated wall-normal fluctuations and enhanced the slip velocities near the wall.

The main challenge with both riblets and permeable walls is their relatively modest velocity range of effectiveness towards drag mitigation for a given configuration. Compliant walls have gained significant interest in flow control as they create a unique opportunity for drag reduction because of the two-way coupling between the flow and solid surface that could be leveraged to broaden the effectiveness envelope. Research in this topic was almost exclusively done with incompressible aqueous flows. Early works on this topic focused on stability of laminar flows over compliant coatings. Landahl [18] and Carpenter and Garrad [19,20] showed that compliant walls may be effective in delaying transition by attenuating the Tollmien Schlichting wave growth for a narrow range of coating parameters, provided that flow-induced structural instabilities are avoided. Duncan [21] qualitatively analyzed the response of a viscoelastic coating to turbulent pressure fluctuations and showed that the flow-induced surface instabilities can be avoided for a narrow range of damping and stiffness combinations. Noteworthy evidence on the drag reduction with viscoelastic coatings was provided by Lee *et al.* [22]. The authors also observed the drag reduction is accompanied by an increase in the near-wall streak spacing and an upward shift of the log layer; these features have also been observed for flows over drag reducing riblets and permeable walls. Choi *et al.* [23] tested highly stiff compliant coatings over a slender body of revolution and obtained a drag reduction of 7%; concomitantly, a reduction in turbulent fluctuations were also observed. DNS studies have also been performed to investigate turbulent boundary layer interactions with nonrigid surfaces at relatively modest Reynolds numbers. Xu *et al.* [24] and Kim and Choi [25] used a distributed spring damper system to model the viscoelastic coating; however, no drag reduction was observed in their works. Using comparisons from active control, Xu *et al.* [24] argued that the phase relation between wall pressure and wall-normal velocity is unfavorable to counteract the ejections and bursts associated with streamwise vortices. Kim and Choi [25] reported the presence of quasi-two-dimensional (2D) waves and increase in drag as the coating became softer. Recent experimental investigations by Zhang *et al.* [26], Wang *et al.* [27], and Greidanus *et al.* [28] have shown that the deformations of the compliant walls are driven by pressure fluctuations in the log-layer. Numerical simulations by Rosti and Brandt [29] for turbulent flow over hyperelastic wall showed the signature of spanwise Kelvin Helmholtz structures as the wall became softer, similarly to flows over permeable walls. All the above studies observed spanwise oriented advected modes in the coating and an increase

in Reynolds stress with increasing flow speeds. Given the diverse observations with the compliant walls, it is apparent that the near-wall turbulent structure over a compliant wall is not yet well understood, and there is a lack of consistency over different experimental and numerical findings regarding its drag reduction effect.

It should be noted that the previous studies on compliant walls have predominantly focused on low-speed aqueous flows. As a notable exception, Pham *et al.* [30] demonstrated that nonrigid surfaces generated by implanting rubber inserts beneath the flow can substantially reduce the shock-induced separation scales in a Mach 2.5 air flow. Walz and Narayanaswamy [31] significantly expanded the separation size range investigated by Pham *et al.* and demonstrated that the rubber implants are effective in mitigating separation scales of the order 10 times the incoming boundary layer thickness, which is representative of practical separation scales observed in internal flows. Interestingly, the authors also reported a concomitant decrease in the skin friction coefficient (C_f) of the turbulent boundary layer over the viscoelastic implant measured at a specific station considerably downstream of the implant leading edge. The reduction in C_f increased with decreasing material Young's modulus (increasing softness) and a maximum reduction of 11% was documented with the softest material implant that was employed.

While the work by Walz and Narayanaswamy [31] is indeed an important demonstration of the potential for using nonrigid (viscoelastic) surfaces for drag mitigation in supersonic flows, there are a few gaps in that study that precludes obtaining a comprehensive evaluation of the drag mitigation using viscoelastic implants and its underpinning mechanisms. First, the C_f measurements were made at one fixed station over implant, which provides little information about how the C_f evolves with downstream distance along the viscoelastic surface. For example, it would be interesting to know if the drag mitigation action of the viscoelastic implant is biased to certain regions along its length. Second, the C_f was determined indirectly from the boundary layer profiles using standard fits. While this fit-based approach is acceptable for most canonical turbulent boundary layers, a more direct method of measuring C_f can provide an independent redundant measurement of C_f and also a more general approach to make C_f measurements in noncanonical boundary layers where effects of viscoelastic coatings may be studied. Finally, the possible mechanisms that resulted in the C_f reduction was not addressed in Walz and Narayanaswamy [31]. Therefore, it is unclear if the discussions made so far in low-speed aqueous flows is transferable to high speeds.

The present work addresses the aforementioned shortcomings of Walz and Narayanaswamy [31]. A direct measurement of the skin friction coefficient was made using oil film interferometry technique and the measured value is compared with redundant measurements obtained using boundary layer profile fits. Furthermore, the C_f was measured at multiple stations along the length of the implant to capture the streamwise evolution of C_f. Finally, a combination of particle image velocimetry (PIV) measurements of turbulent statistics in the boundary layer and analysis of material deformation spectra were made to explain some of the possible underpinning mechanisms that are responsible for C_f reduction.

II. EXPERIMENTAL SETUP

A. Test facility and model

The experiments were performed in a variable Mach number supersonic wind tunnel at North Carolina State University; the freestream Mach number for the present study was set at 2.5. The wind tunnel is a blowdown type facility with 10 s of run time that provides freestream pressure with less than 2% drift. The test section measured 150×150 mm in cross section and 650 mm in length. More details about the tunnel operation can be found in the earlier works on this facility [32–35]. For the current experiments, the stagnation pressure and stagnation temperature were set at 544 kPa and 298 K, respectively. This resulted in a freestream velocity of 580 m/s and unit Reynolds number of 27×10^6/m, respectively.

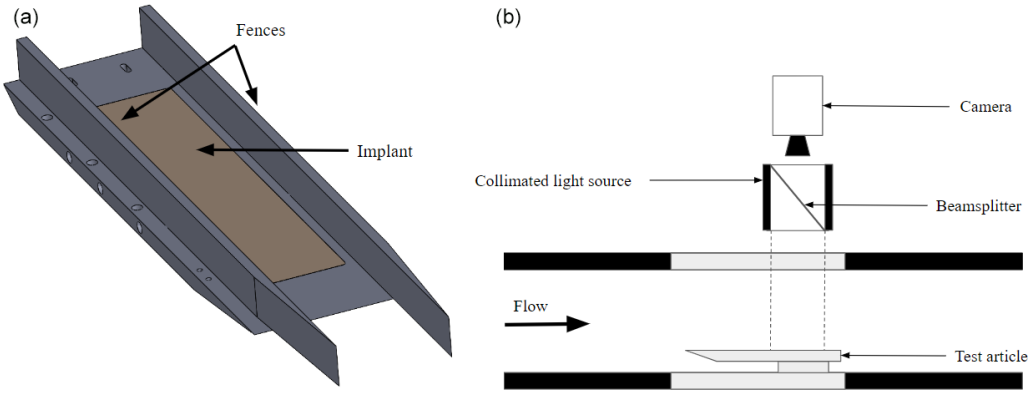

FIG. 1. (a) Schematic of the test article used for the present study and (b) illustration of the experimental setup for oil film interferometry technique.

The test article [schematic in Fig. 1(a)] consisted of a steel plate [355.6 mm (l)×101.6 mm (w)×10.5 mm (t)] with a sharp leading-edge and two side fences (25 mm tall) that extended along the length of the plate. These side fences helped arrest the spanwise flow caused by the vortex roll up along the sides of the plate. However, the boundary layers that develop along the junction between the plate and the side fences caused a small fluid motion towards center span of the plate, which were noticeable in surface streakline visualization images. The test article was placed in the freestream at nominally zero pitch and yaw angles for all the experiments. This allowed a fresh boundary layer to develop along the plate and side fences. The boundary layer naturally transitioned to turbulence within a short distance from the plate leading edge. For the present work, the origin will be located at the intersection of the plate leading edge ($x = 0$), plate midspan ($z = 0$), and plate surface ($y = 0$), and the flow is along the positive x direction.

A 4-mm(t) deep recess [250 mm (l) × 57 mm (w)] was made on the plate starting at $x = 50$ mm to allow the viscoelastic surface to be implanted into the plate; the depth of the recess was sufficient to realize the bulk properties of the inserted materials. We refer to this configuation as C_1, and is shown in Fig. 1(a). Polyurethane rubbers of different shore hardness were used as viscoelastic materials. Two different rubbers were used in the present study with shore hardness of 60A and 20A. The elastic modulus of the rubber implant materials is listed in Table I. For manufacturing both these rubber inserts, ReoFlex polyurethane series was used. These were two-part liquid pour rubbers that naturally adhered to the steel during the curing process. After the rubber was poured into the recess, the model was placed in a vacuum oven to go through multiple cycles of degassing process before curing. The mean undulations of the surface [$w(x, z)$] after curing were mapped using a 3D profilometer (Filmetrics Inc., model: Profilm3D) by Walz and Narayanaswamy [31] and their values are reported here because of the identical procedure and materials employed between the two works. The undulation map over 1.5×1.5 mm area by Walz and Narayanaswamy [31] revealed a smooth finish and the spatial rms undulation collecting $w(x, z)$ across the spatial domain was 0.49 μm, which was well below the roughness limit of the boundary layer.

TABLE I. Material properties of rubber.

Hardness	(kPa) Storage modulus (E')	(kPa) Loss modulus (E'')	(kgm^{-3}) Density (ρ_w)	(ms^{-1}) Shear speed (C_t)
60A	2100	250	1040	25.4
20A	840	250	1010	17

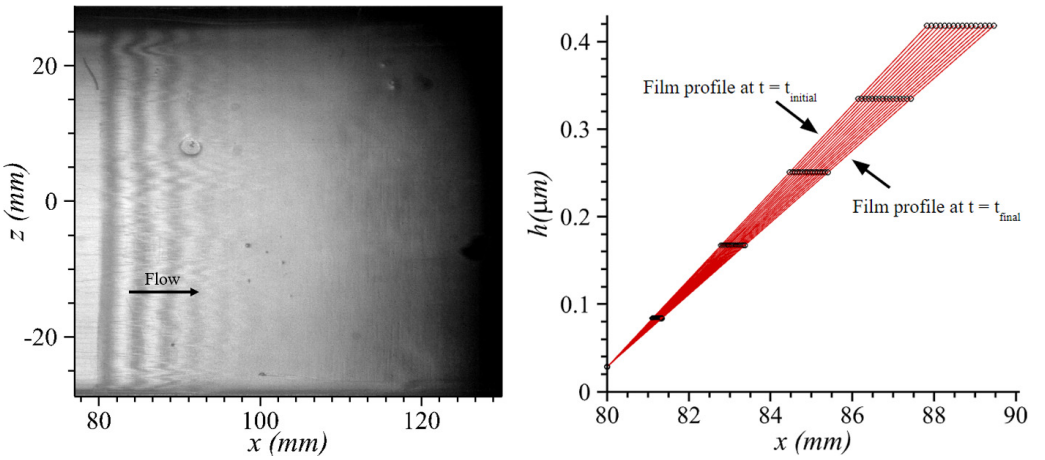

FIG. 2. (a) A sample snapshot of the imaged fringes using the OFI technique and (b) Linear fits of the oil film height along the streamwise direction at different time instances.

B. Oil film interferometry setup and processing

Oil film interferometry (OFI) technique was employed to provide a direct measurement of the wall shear stress from which the skin friction coefficient, C_f, was obtained. A detailed description of the technique and its application in different flow configurations are provided in Naughton and Sheplak [36]. In summary, this technique uses the optical fringe pattern formed by an oil film undergoing shear thinning to determine the corresponding wall shear stress. The governing equation for oil film undergoing one-dimensional shear thinning is given by

$$\frac{\partial h}{\partial t} = \frac{\partial}{\partial x}\left(\frac{\tau_x h^2}{2\mu}\right). \tag{1}$$

Here $h = h(x, t)$ is the instantaneous oil film height, μ is the dynamic viscosity of the oil film, and x is the streamwise direction. Integrating Eq. (1) in time and marching in the streamwise direction, τ_x, for a given grid index $i + 1$ along the streamwise direction, can be evaluated using the following equations:

$$\underbrace{h(t_2) - h(t_1)}_{B} + \frac{\partial}{\partial x}\frac{\tau_w}{2}\underbrace{\int_{t_1}^{t_2}\frac{h^2}{\mu}dt}_{A} = 0, \tag{2}$$

$$\tau_w^{i+1} = \left(\tau_w^i A^i - 2\Delta x B^{i+1/2}\right)\Big/ A^{i+1}. \tag{3}$$

To implement this technique, the test article was coated with a low-viscosity silicone oil (Sigma Aldrich Inc., $\nu = 50\ cSt$). The oil coating was allowed to be sheared by the wind tunnel flow to result in a very thin film that generated the interference pattern. Due to the relatively short tunnel runtime of the wind tunnel facility, low-viscosity oil was used owing to their shorter fringe development times and a larger fringe spacing (Schulein [37] and Hubner and Carroll [38]). A schematic of the optical setup is shown in Fig. 1(b). A collimated blue light source (Metaphase Inc., model: MB-DAL 404) illuminated the test article to cause optical interference. An interline CCD camera captured the interference fringe development at 30 frames per second in a direction perpendicular to the model surface. This acquisition rate was sufficient to time resolve the transient evolution of the fringes to a steady state, which took about 3 s of the run time; a total of 210 frames are obtained for a 7-s test run to provide about 60 frames during the steady state of fringe development. Five test runs were performed for each measurement point.

Figure 2(a) shows a typical instantaneous fringe pattern during the steady state of fringe development. During this steady-state operation, the fringes exhibited a slow downstream motion with their topological pattern unchanged. As observed from Fig. 2(a), the images exhibit excellent contrast to make a clear identification of the regions with constructive and destructive interference and enables a clear examination of the topological features of the fringe patterns. Furthermore, the fringe patterns are spanwise aligned and straight over 60% of the spanwise length. Some curvature in the fringes can be noticed towards the spanwise edges of the plate, which is likely caused by the presence of the junction boundary layer along the intersection between the plate and the side fences.

For data processing, the multi-image analysis described by Naughton and Hind [39] was used since it is insensitive to tunnel startup transients and more robust than other techniques. Since shear stress was evaluated along the streamwise direction, the spatial domain of interest was discretized uniformly starting from the leading edge of the oil film. Figure 2(a) shows that the first fringe formed is a dark fringe, where the oil film height given by $h = \frac{\lambda}{4n_f}$ for normal light incidence. Here λ is the wavelength of the incident light and n_f is the refractive index of the oil. Moreover, the oil film height corresponding to the jth fringe is given by

$$h_j = \frac{j\lambda}{4n_f}. \tag{4}$$

Using Eq. (4) and the data reduction technique from Naughton and Hind [39], the spatial height distribution of the oil film for individual snapshots in obtained. Figure 2(b) presents linear fits of the oil film height along the streamwise direction at different time instances. The linear fits were observed to represent the experimental height distributions very well at all time instances. The spatiotemporal distribution of the oil film height was subsequently averaged between -10 mm $< z < +10$ mm before it was incorporated into Eq. (3). The corresponding spatiotemporal distribution of the wall shear stress was obtained by numerically solving Eq. (3). Each sample of wall shear stress data is therefore a spatiotemporal average over the extent of fringe coherence ($\approx$5–10 mm) in the streamwise direction, 20 mm in the spanwise direction, and 30 time snapshots. This resulted in at least 10 uncorrelated wall shear values for each measurement location. The corresponding skin friction coefficient, C_f, was obtained from the wall shear stress field at a given streamwise location.

The quality of the C_f measurements was determined by the ability to obtain high dynamic range between the dark and bright fringes to clearly identify their respective locations. This was in turn dictated by the state of the oil film at particular instance, reflectivity of the implant surface, and the fringe decoherence due to the finite spectral width of the incident light (10 nm). Based on these considerations, the uncertainty of the C_f measurement was determined using the lower and upper bounds of the oil film height distribution across different datasets. Based on over 30 such oil film height distributions, the uncertainty in C_f is estimated to be 5% over the rigid surface and 11% over the rubber implants.

For skin friction measurements, two different test configurations have been used to understand the evolution of C_f over viscoelastic implants. The details of the first configuration (C_1) had been discussed in Sec. II A and shown in Figure 1(a), where the viscoelastic patch was present over the entire length of the recess. In this configuration, there could be two scenarios where OFI may provide inaccurate results. First, highly unsteady surface deformations of the rubber implant may interfere with the natural thinning rate of the oil. Second, the adhesion characteristics between silicone oil and polyurethane rubbers are not known and may change the natural oil thinning rate. To circumvent these concerns, a second configuration (C_2) is considered as shown in Fig. 3, where the rubber implant extended only up to 120 mm from the leading edge of the recess (i.e., until $x = 170$ mm). The remaining 130 mm of the recess downstream of the rubber was implanted with a rigid plate. C_f measurements were performed at a few closely spaced locations ($x = 175$ mm, 180 and 200 mm) just downstream of the rubber or rigid implant interface to confirm the change in C_f observed from the first configuration, as well as to understand the downstream evolution of the C_f past the rubber implant.

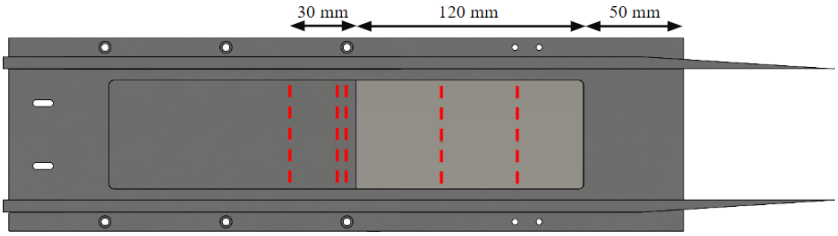

FIG. 3. Schematic of C_2 with measurement locations shown with red dashed lines.

C. PIV setup and processing

PIV was employed to obtain two-component velocity fields in the streamwise wall-normal plane from which the relevant boundary layer statistics and a redundant measure of C_f were obtained. The technique involved illuminating the externally injected neutrally buoyant tracer particles (silicon oil droplets of 0.2–0.3 μm agglomerated size) by two time separated laser sheets ($\lambda = 532$ nm) and imaging the resulting laser scattering by a frame straddling interline CCD camera (PCO Inc., model: PCO2000). The laser and camera timings were controlled and synchronized to within 1 ps using a low -jitter delay generator (Stanford Research Systems Inc, model: DG645). The field of view measured was 73.5×73.5 mm centered around $x = 250$ mm with a digital resolution of 42 μm/pixel. Usable region of interest over which the velocity fields were considered for further processing extended from 230 mm $\leqslant x \leqslant$ 270 mm. Multipass image interrogation was used and the final interrogation window was 16×16 pixels, with a 50% overlap. Median filtering was performed during postprocessing to remove spurious vectors. The processed frames spanned ($8\delta \times 4.8\delta$) with 91×54 vectors at a resolution of 0.35 mm.

Based on our prior comparisons of the mean boundary layer profiles at Mach 2.5 using PIV and pitot probe scans, we obtain a maximum error of ≈ 2% (11 m/s) in the mean velocity values. To quantify the measurement error in the turbulent quantities, the variance of turbulent statistics is calculated as (Priestley [40])

$$\mathrm{var}\left(u_i'^2\right) = \frac{2\sigma_{u_i}^4}{N_F N_K^*}. \tag{5}$$

Here σ_{u_i} is the turbulence intensity of the ith velocity component, N_F is the number of frame pairs, and N_K^* is the number of uncorrelated u_i' samples in each image pair, which is in turn given by

$$N_K^* = N_K \Big/ \sum_{-N_K}^{N_K} \left(1 - \frac{|k|}{N_K}\right) \rho_{ii}^2[k]. \tag{6}$$

Here N_K is the number of nonoverlapping interrogation points in the homogenous direction, which is the streamwise (x) direction in this case, and $\rho_{ii}[k]$ is the autocorrelation function of the ith velocity component in the homogenous direction. The autocorrelation functions of u' and v' fluctuations were approximated as simple exponential functions using the integral length scales obtained from Pirozolli and Bernardini [41], which were approximately 0.8δ and 0.2δ, respectively. Due to the shorter integral length scale, the effective number of indepedent row interrogation points (N_K^*) of v' was significantly higher than that of u'. Finally, a t distribution with 95% confidence bound is used to approximate the error bounds.

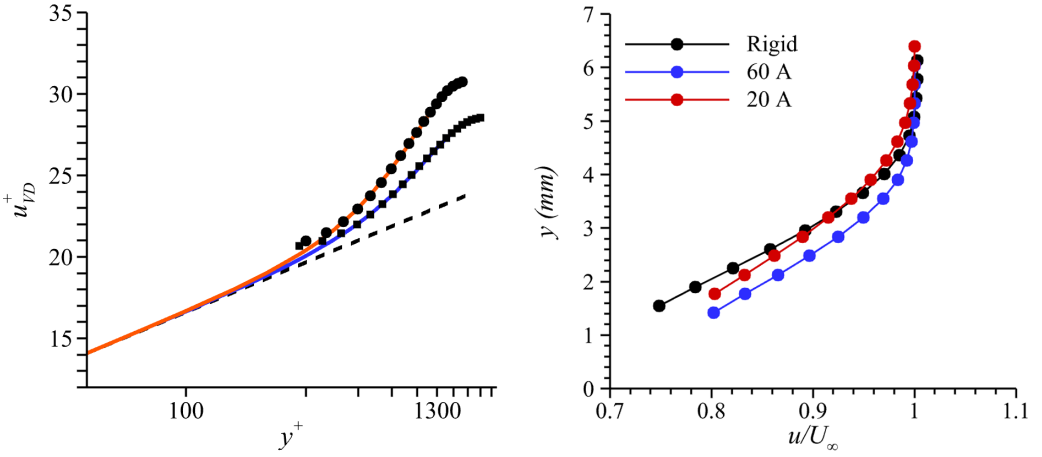

FIG. 4. (a) Mean velocity profiles over rigid and 20A viscoelastic surfaces. Symbols correspond to measurements and solid or dashed lines correspond to theoretical fits. The figure includes ● ● ●, rigid wall; ■■■, 20A viscoelastic surface; ——, theoretical fit for rigid wall; ——, theoretical fit for viscoelastic surface – –, classical log layer line, and (b) raw boundary layer profiles over rigid wall and two different viscoelastic coatings.

III. RESULTS AND DISCUSSION

A. Mean velocity profiles

The mean velocity profiles obtained from PIV measurements were fitted against standard boundary layer profiles. The canonical turbulent boundary layer profile of Coles [42] was used to fit the velocity data. This profile uses the van Driest transformed effective velocity (u^+_{VD}) for an adiabatic wall, which when normalized by the friction velocity (u_τ), is related to the other variables by the following equation:

$$u^+_{\mathrm{VD}} = \frac{1}{\kappa}\log\frac{u_\tau y}{\nu_w} + C + \frac{2\Pi}{\kappa}\sin^2\left(\frac{\pi y}{2\delta_c}\right). \tag{7}$$

Here κ and C are the standard log-layer constants, ν_w is the kinematic viscosity at the wall, Π is the wake strength, and δ_c is the Coles boundary layer thickness. Figure 4(a) shows the measured velocity data, the theoretical fit, and constant slope log layer line in inner units for the rigid wall and 20A rubber cases. It can be observed that the dataset extends down to about $y^+ \approx 250$, which is above the outer edge of the log layer for a typical turbulent boundary layer. Thus, the current datasets provide only the outer layer behavior of the turbulent boundary layer that is being studied. Figure 4(a) shows that the experimentally obtained velocity data align strongly with the canonical fit for both the rigid wall and the 20A rubber implant cases. This strong agreement was also observed with the 60A rubber implant, which suggests that the viscous implants do not alter the fundamental canonical nature of the turbulent boundary layer, at least in the outer region. Figure 4(b) shows the raw boundary layer profiles over the three different cases considered. The relevant boundary layer parameters are listed in Table II.

B. Skin friction

Skin friction coefficients obtained using the OFI are presented in Figs. 5(a) and 5(b) for both configurations C_1 and C_2 along successive streamwise stations. Measurements made with 60A and 20A rubber implants are presented to delineate any trends with implant softness that could be captured from the measurements.

TABLE II. Boundary layer parameters.

Wall type	$E'/\rho_\infty U_\infty^2$	δ_{99}(mm)	δ^*(mm)	θ (mm)	Re_θ	Re_τ	C_f
Rigid		4.50–0.5	1.74	0.416	18630	1630	0.0011
60A	2.24	4.12–0.56	1.42	0.346	15655	1688	0.0013
20A	0.87	4.91–0.71	1.67	0.413	18401	1867	0.0013

The C_f over the rigid plate shows a decreasing trend with downstream distance starting at 1.55×10^{-3} at $x = 80$ mm down to 1.3×10^{-3} at $x = 250$ mm. This trend qualitatively matches the theoretical predictions for a canonical turbulent boundary layer. The corresponding C_f for the full length rubber implants (C_1) are shown in Fig. 5(a). At $x = 80$ mm, the C_f is measured to be 1.05×10^{-3} and 1.15×10^{-3} for the 60A and 20A rubbers, respectively. These values represent a 32% and 26% reduction in C_f compared to the rigid plate configuration at $x = 80$ mm. After this steep decrease measured at $x = 80$ mm, the C_f values exhibit an overall decreasing trend with downstream distance for both the implants. The skin friction coefficient with the 20A rubber implant reaches a global minimum value of $C_f = 0.85\times10^{-3}$ at $x = 200$ mm while the corresponding value for the 60A rubber implant is 0.9×10^{-3} at $x = 170$ mm. While notable nonmonotonic variations in C_f with downstream distance can be observed in Fig. 5(a), which conflicts with theoretical evolution of C_f along a canonical flat plate boundary layer, we believe that these variations are within the error bounds of the technique; therefore, these trends are not considered significant in this work.

The corresponding C_f for the half length rubber implants (C_2) are shown in Fig. 5(b). The first two measurement stations are over the implants, and have values that are within the error bound of those observed with C_1 configuration presented in Fig. 5(a). Therefore it can be concluded that changing the length of the implant by almost 50% did not change the C_f. As the wall transitions from nonrigid to rigid surface at $x = 170$ mm, the C_f values for both rubbers are found to increase. For 60A configuration, the C_f at $x = 175$ mm is 1.15×10^{-3}, which is 20% lower than the corresponding C_f for the rigid plate. In case of 20A implant, the C_f measured at $x = 175$ mm is higher than 60A but still about 14% lower than the corresponding rigid case. The higher C_f of the 20A implant compared

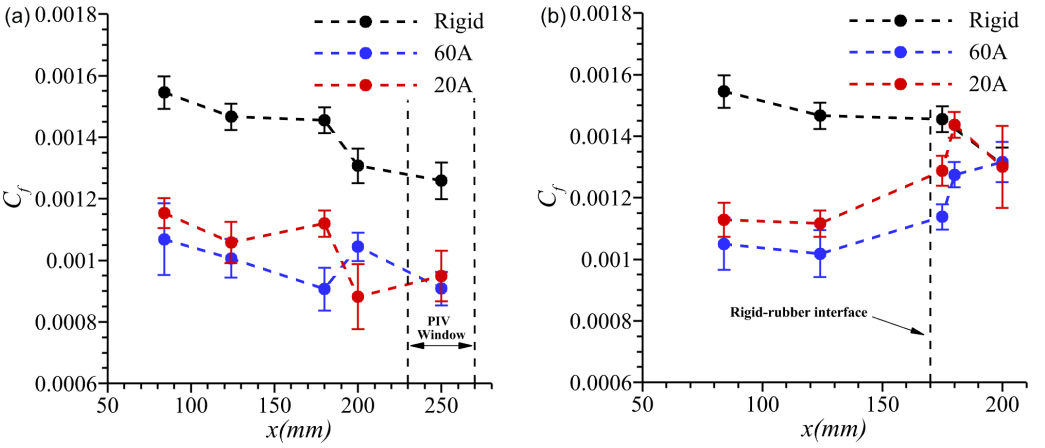

FIG. 5. Measured C_f variation along the streamwise direction over rigid and viscoelastic surfaces for (a) Configuration C_1 and (b) Configuration C_2. The error bar at corresponds to the 99% confidence interval obtained using the t distribution of the C_f for the given location and material setting.

to the 60A implant at $x = 175$ mm seems to be a continuation of the same trend observed all along the implant. Further downstream ($x > 175$ mm), the C_f for both rigid and 60A implant show a rapidly increasing trend and eventually converge to the C_f over the rigid surface. Interestingly, the C_f for 20A implant is found to converge with the rigid wall C_f quicker than the 60A implant. Overall, the current set of measurements made on both C_1 and C_2 test configurations demonstrate that the C_f measured over both the implants using the OFI technique is indeed lower than the rigid case. Once the boundary layer crosses into the rigid surface, the C_f increases rapidly as the boundary layer adjusts to the change in wall boundary conditions from nonrigid to rigid.

Redundant C_f values from the boundary layer velocity fits averaged over 230 mm $\leqslant x \leqslant$ 270 mm is presented in Table II for the rigid plate and the two rubber implants. Comparison of the mean profile fit and OFI-based C_f for the rigid surface at $x = 250$ mm shows that the fit-based C_f value is about 15% smaller. This level of agreement is quite encouraging as it lies well within the experimental uncertainty of C_f obtained using the OFI technique. The C_f values for the rubber implant cases obtained using boundary layer fit and the OFI technique at $x = 250$ mm, however, deviate by 44% and 33%, respectively, for the 60A and 20A implants. In fact, whereas the fit-based C_f estimates a slight increase in C_f with 60A and 20A rubber inserts, the OFI-based C_f measured a decrease in C_f. While this conflict cannot be resolved presently owing to the lack of another set of independent measurements, we note that the measured C_f decrease at $x = 250$ mm using the OFI technique is above the error margin of the OFI technique. It is also important to point out the boundary layer fit for the inner layer made while calculating the C_f from velocity measurements may be deficient; notably, the C_f values have a critical dependence on the inner layer model employed. We further note that the decrease in C_f with the implants over the locations 80 mm $\leqslant x \leqslant$ 150 mm is greater than the difference in C_f between the PIV and OFI-based approaches obtained at $x = 250$ mm shown in Fig. 5(a) and Table II. These observations strongly suggest that there is indeed a considerable reduction in the C_f in the presence of a rubber implant at least over a substantial length of the implant.

In summary, there is a remarkable decrease in C_f for the boundary layers over the rubber implants over $x \geqslant 80$ mm that is beyond the measurement error margins of the OFI technique. Interestingly, this location, $x = 80$ mm, is only 30 mm from the leading edge of the rubber insert. This means that the boundary layer adjusts to the new (nonrigid) wall conditions offered by the implants rapidly and a decrease in C_f occurs within a short distance into the implant, after which the evolution of C_f is gradual. From a practical drag mitigation standpoint, this result supports using short and optimally placed patches of viscoelastic implants for the best outcome. In the following sections, a detailed investigation into the underpinning interactions that result in the observed C_f reduction is made.

C. Mean boundary layer properties

The boundary layer parameters are presented to learn how the presence of rubber implants modify the aggregate boundary layer properties. Table II lists the boundary layer thickness obtained at $x = 240$ mm based on 99% freestream velocity over rigid and different implants. The boundary layer thickness for the 60A implant exhibits a slight decrease compared to the rigid surface, while the boundary layer thickness for the 20A implant exhibits a slight increase compared to the rigid surface. The displacement and momentum thicknesses for 60A implant are also lower than those of the rigid surface, whereas those of 20A implant are similar to the rigid surface values. These observations can be contrasted with the noticeable thickening of the boundary layer observed over permeable walls [13] and flexible walls [29] with increasing permeability and flexibility. This general trend of boundary layer thickening with increasing softness is not observed in the present study. Given that the overall integral boundary layer properties are quite similar between the rigid surface and rubber implants, the question is if the turbulent statistics of the boundary layer gets modified by the rubber implants; this will be addressed next.

D. Turbulent fluctuations

In this section, the rms profiles of the fluctuating streamwise (u'), wall-normal (v') velocity components, and Reynolds stress component ($-u'v'$) are individually presented in Fig. 6, along with their density scaled values. The profiles are normalized by the friction velocity for the rigid wall configuration u_τ^r to make consistent comparison with the literature. This normalization also provides a physical comparison of the values between the rigid and rubber implant configurations.

The streamwise rms velocity (u') profiles are shown in Figs. 6(a) and 6(b). Considering the rigid case first, it is observed that the freestream u' is about 10% of the u_τ^r in the vicinity of the boundary layer edge, which is in line with the values reported in Hou [43] as well as the estimated freestream turbulence of 0.1% u_∞ or 6% u_τ^r. Furthermore, the measured u' profiles for the rigid case agree within 10% of the corresponding profile obtained from the DNS of supersonic boundary layer at $\mathrm{Re}_\tau = 1120$ by Pirozzoli and Bernardini [41]. The difference in u' profiles between rigid and 20A rubber implant case different rubbers is minor throughout the boundary layer over the measurement domain, while a slight decrease is observed for the 60A rubber.

The wall-normal rms velocity (v' normalized by u_τ^r) profiles are presented in Figs. 6(c) and 6(d). The (v'/u_τ^r) profiles in Fig. 6(d) agrees well with the data of Elena and Lacharme [44]; however, the measured profile was about 25% lower than the DNS-based v'/u_τ^r of Pirozzoli and Bernardini [41]. Comparing the v'/u_τ^r between the rigid and rubber implant configurations, one can observe a pronounced increase in v'/u_τ^r for the 20A rubber implant configuration compared to the rigid plate, while the corresponding value of the 60A rubber implant is marginally lower than the rigid plate configuration. This difference in the v' for 20A implant configuration widens with decreasing y location and a maximum increase of 23% was observed at the measurement station closest to the wall ($y/\delta = 0.4$). The Reynolds stresses profiles across the different configurations are presented in Figs. 6(e) and 6(f), where a strong difference is observed between the rigid plate and rubber implants, whereas a reduction of 35% was observed in the innermost point for the 60A rubber implant, an increase of 16% was observed for the 20A rubber implant at the same location. The Reynolds stress profiles for both the implants rapidly approach the rigid plate profile for $y/\delta \geqslant 0.7$.

Previous numerical and experimental studies on hyperelastic walls in incompressible flows by Rosti and Brandt [29] ($\mathrm{Re}_\tau = 200$) and Wang *et al.* [27] ($\mathrm{Re}_\tau = 1400$–5000) showed a monotonic increase in the turbulent velocity fluctuations with increasing wall compliance, whereas the increase in v', w', and Reynolds stress were the most prominent, streamwise fluctuations also increased modestly. Comparing the literature values with the present study, it is noted the 20A rubber ($E'/\rho U^2 = 0.87$) exhibited a maximum increase of 23% in the v' values compared to the 200% increase calculated by Rosti and Brandt [29] with a very similar $E'/\rho U^2 = 1$. Similarly, whereas the flow over the 60A implant ($E'/\rho U^2 = 2.24$) exhibited only a marginally lower v' profiles compared to the rigid plate, a 25% increase in the wall-normal fluctuations was noted by Wang *et al.* [27] with $E'/\rho U^2 = 2.76$. These differences evidence a much smaller increase of the wall-normal and streamwise velocity fluctuations in the present study compared to the literature for comparable values of $E'/\rho U^2$. We posit that the observed difference is primarily an effect of using air as the working fluid. The effect of using air as the working fluid can be understood by considering a nondimensional parameter called implant to fluid mass ratio (C_M), given by

$$C_M = \frac{\rho_w d_0}{\rho_f \delta}. \tag{8}$$

Here ρ_w is the implant density, d_0 is the implant depth, ρ_f is the fluid density, and δ is the boundary layer thickness. For the present study, $C_M = O(10^3)$, whereas in incompressible aqueous flows studied by Wang *et al.* [27], $C_M = O(1)$. Using resolvent analysis, Luhar *et al.* [45] showed that in comparison to aqueous flows, the peak response of compliant walls in gas flows is highly restricted to a narrow band around resonance, dropping sharply outside the resonant frequencies. This large disparity in the C_M at at least partly explains the reduced changes in wall-normal fluctuations and Reynolds shear stress. In summary, the turbulent fluctuation profiles reveal disparate statistics in

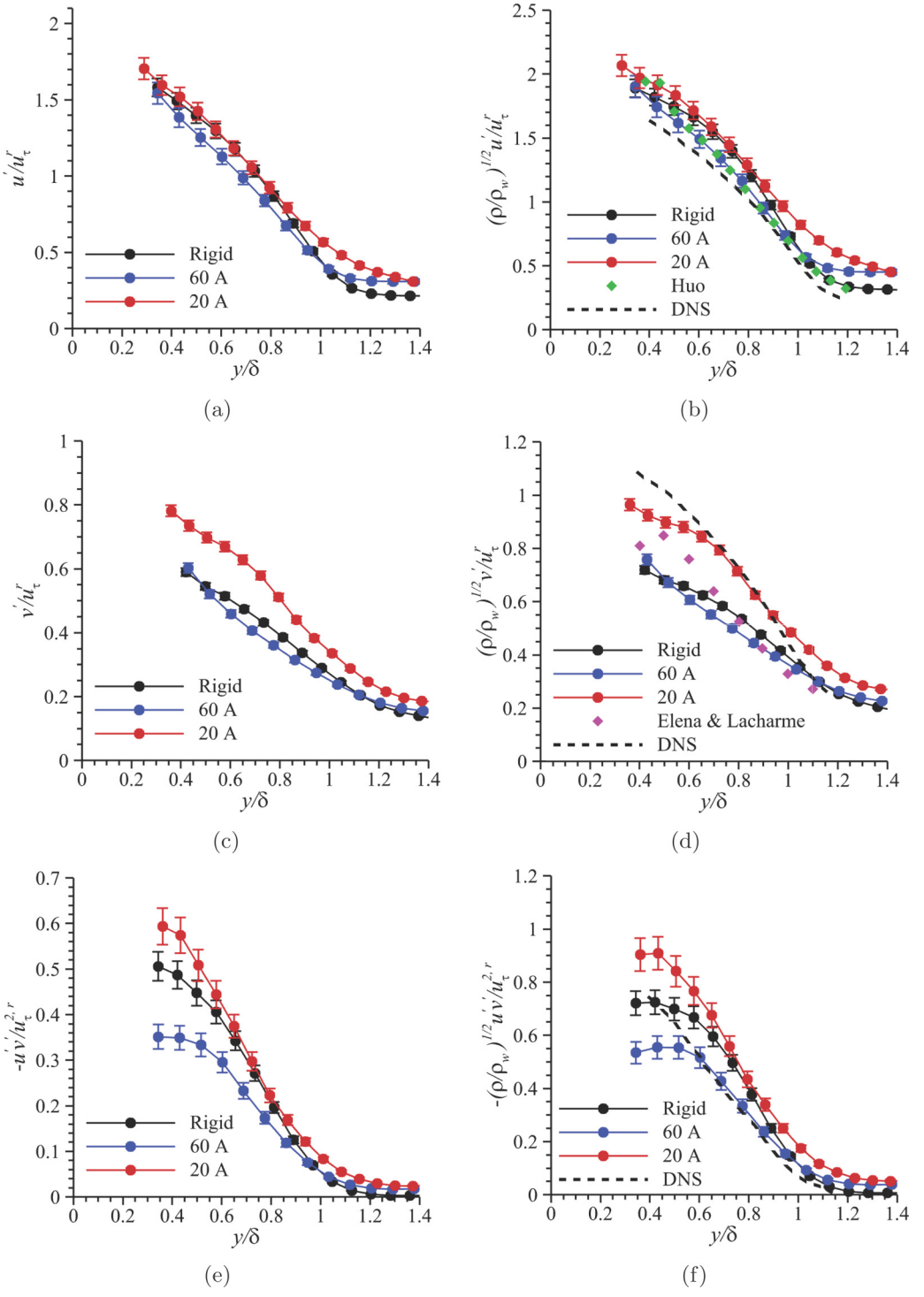

FIG. 6. [(a), (c), and (e)] Wall-normal profiles of the streamwise velocity fluctuations (u'), wall-normal velocity fluctuations (v'), and Reynolds shear stress ($-u'v'$). Profiles are scaled by friction velocity of the rigid surface (u^r_τ). Panels (b), (d), and (f) consist of the same quantities but scaled using local density.

the outer region between the two rubber implants; interestingly, both these implants generate a very similar reduction in the C_f. This fact points to the potential modifications in the near-wall turbulence by these implants as the possible drivers of skin-friction mitigation. The following discusses some of the possible mechanisms that drive these near-wall interactions from a theoretical or analytical framework.

IV. DISCUSSIONS

A. Onset of surface instability waves

One of the possible interaction mechanisms could be the two-way coupling between surface instabilities and the surrounding flowfield, resulting in noticeable flowfield outcomes (Gad el Hak *et al.* [46] and Gad el Hak [47]). These coupled interactions can result in the development of unstable waves over the viscoelastic surface, which can strongly affect the turbulent statistics and skin friction coefficient. Duncan [21] examined the wave characteristics of a viscoelastic coating subjected to turbulent pressure fluctuations and obtained a neutral stability curve as a function of the material damping of the viscoelastic coating and a nondimensional parameter U_c, defined as the ratio of freestream velocity and the material shear speed $U_c = U_\infty/C_t$.

For viscoelastic coatings with low damping, the most commonly observed instability is known as traveling wave flutter, where an unstable wavetrain propagates in the flow direction at speeds close to the material shear speed. Gad el Hak [47] experimentally observed traveling wave flutter on an elastic coating of very low damping and found the wave amplitudes to be of the order of a millimeter, which is significant enough to alter the boundary layer turbulence characteristics. The analysis of Duncan was adopted in the present study to generate the neutral stability curve for air flow as the working medium and reproducing the freestream velocity and density conditions of the experiments. Based on this analysis, both 60A and 20A rubber implants are not expected to develop unstable surface waves. This was also confirmed in our experiments where no undulations were observed from laser scattering off the implant surface in the raw images used for PIV.

For viscoelastic coatings with large internal damping, a slow moving unstable wave system called static divergence has been observed by Gad el Hak [46] and Hansen and Hunston [48]. The crests of these unstable waves in Gad el Hak *et al.* [46] extended into the outer layer and behaved as surface roughness that substantially increased the skin friction drag. The onset of static divergence waves was also calculated from the neutral stability curves of Duncan [21]. The calculations reveal that the onset of these static divergence waves occurs above a threshold value of $U_c > 2.85$. In the present study, the value of U_c was determined to be 0.66 and 1.07 for the 60A and 20A rubber implants, respectively, which places both the implants well below the possibility of the occurrence of static divergence waves; this was also confirmed by our experiments. Thus, the theoretical analyses as well as experiments confirm that both rubber implants belonged to the stable regime where the flow-induced surface instabilities would not grow or propagate.

B. Resonant coupling of surface vibrations

The above discussions place the spotlight on the possibility of resonant coupling between the implant surface vibrations and near-wall turbulence activities. To evaluate the strength of these interactions, we estimated if the implant surface vibration amplitudes are large enough to impact the near-wall activities and if one or more vibration modes lie in the frequency range that can impact the dominant turbulence activities.

The governing equations of a linear isotropic viscoelastic solid is given by (Landau *et al.* [49])

$$\rho\ddot{\mathbf{s}} = \frac{E}{2(1+\sigma)}\Delta\mathbf{s} + \frac{E}{2(1+\sigma)(1-2\sigma)}\nabla(\nabla.\mathbf{s}). \tag{9}$$

Here ρ is the density of the material, $s = [s_1, s_2, s_3]^T$ is the deformation vector, $E = E' + iE''$ is the complex elastic modulus of the viscoelastic material, and σ is the Poisson's ratio. The viscoelastic

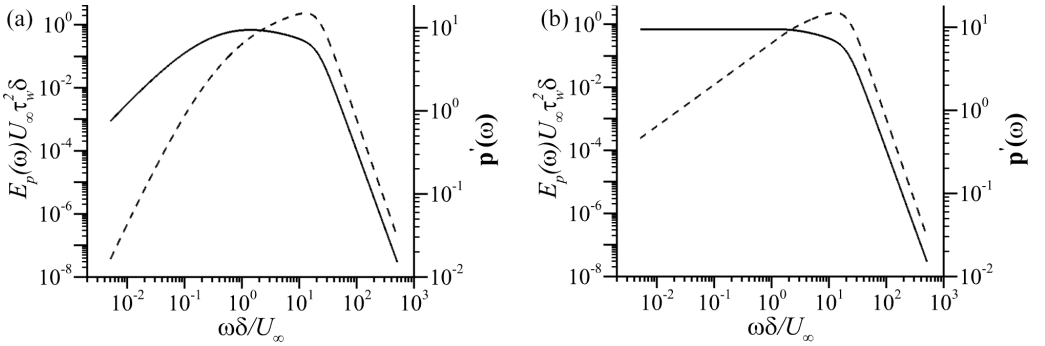

FIG. 7. Model wall pressure spectra that will be used as an input to calculate the viscoelastic surface response to the unsteady normal stress caused by the wind tunnel flow: (a) Goody's model and (b) modification using Beresh's data; —, normalized premultiplied wall pressure spectra; and − − −, wall pressure fluctuations in physical units.

patch is fixed at the bottom and subjected to normal stress at the top. The displacement field is assumed to be homogenous in streamwise and spanwise directions, as well as in time. Hence, using Fourier transform in (x, z) and Laplace transform in time, the deformation can be written as

$$s = \hat{s}(y)e^{i(k_x x + k_z z - \omega t)}. \tag{10}$$

Here (k_x, k_z) are the wave numbers in the x and z directions and ω is the angular frequency. Expressing the deflection vector in the form of Eq. (10) reduces Eq. (9) into an ODE with only the wall-normal (y) coordinate as the dependent variable. The resulting equation was solved using a Chebyshev collocation method. The fluctuating normal stress input on the outer surface was the turbulent wall pressure fluctuations, which was obtained based on Goody's [50] empirical model. The premultiplied wall pressure spectra normalized by wall shear stress (τ_w) obtained from Goody's [50] model is shown in Fig. 7(a). The frequency in the x axis is normalized in terms of characteristic boundary layer frequency (U_∞/δ). Comparing the model spectra from Goody [50] with the experimental spectra from Beresh *et al.* [51], it was observed that Goody's [50] model spectrum has a low-frequency roll-off that is proportional to ω^2, which was absent in experiments. As a result, for the present calculations, the Goody's [50] model spectra was modified to have a flat spectrum at the low frequencies while keeping the remaining part of the scaling unchanged from Goody's [50] model; the modified wall pressure power spectra is shown in Fig. 7(b).

The frequency-dependent normal stress was applied as the input and the governing equations (9) were solved for a range of flow relevant streamwise wave numbers and frequencies. The fluctuating deformation amplitude contours over a range of frequencies and streamwise wave numbers (k_x, ω) for the spanwise constant $(k_z = 0)$ mode are shown in Fig. 8 for the 60A and 20A implants. The wave number in the x axis is scaled both on the implant thickness (d_0) as well as the boundary layer thickness (δ). Similarly, the frequency in the y axis is normalized both in terms of characteristic boundary layer frequency (U_∞/δ) as well as the characteristic material frequency based on its shear speed and thickness (C_t/d_0).

Figure 8 shows that the spectral contours for both the 60A and 20A implants are qualitatively very similar. The peak deformation amplitude is observed to occur along a distinct curve spanning across the entire wave-number range. This peak deformation contour corresponds to the first natural mode of vibration of the implant. Multiple natural modes of vibration whose resonance frequencies exhibit a similar dependence on the spatial wave number can be observed in Fig. 8 for the 60A and 20A implants; however, the deformation amplitude curves at different resonant modes are diffuse in the 20A implant due to its higher damping. An important wave number in the resonance curve of the first mode is the region of maximum deformation, which occurs at $kd_0 = \frac{2\pi}{3}$. This surface

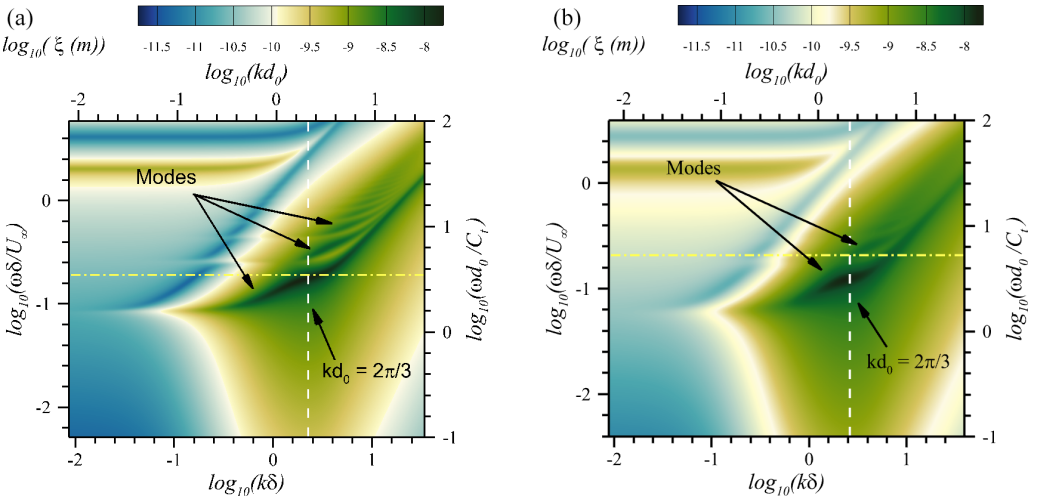

FIG. 8. Calculated deformation spectra for spanwise uniform mode ($k_z = 0$) for (a) 60A and (b) 20A rubber implants in response to the unsteady normal stresses modeled as a modified Goody's [50] spectrum. The vertical dashed line represents the wavelength of maximum deformation and the horizontal dash-dotted line represents the mean burst frequency as reported by Blackwelder [52].

undulation wave number has also been observed to be dominant in the experiments of Wang *et al.* [27]. Maximum deformation amplitudes at higher modes are also observed within the same order of magnitude as $kd_0 = \frac{2\pi}{3}$. Now the question is if the resonant vibrations for a given elastic mode can interfere with the turbulent activities.

To address the aforementioned question, we examine if the resonant vibrations of the rubber implant surfaces can interfere with turbulent bursting cycles by studying the overlap between the surface vibration frequencies and the turbulent burst cycle frequency. The turbulent bursting events are not random but occur over a band of frequencies. The appropriateness of scaling the burst frequency to outer versus inner variables is still being debated. In the present study, the results of Blackwelder [52] was used since it has the closest momentum thickness-based Reynolds number ($\mathrm{Re}_\theta = 10\,000$) to the current experiments ($\mathrm{Re}_\theta = 15\,000$). The mean burst frequency obtained by Blackwelder [52] scaled on inner variables and was calculated to be $\approx 0.0035\, u_\tau^2/\nu$. Applying this relation for the present study, the mean bursting frequency of the near-wall structures was calculated to be $f_b = 22$ kHz. Given that the burst frequency spans a range of values surrounding the mean burst period, we examine the resonant frequencies of the rubber implants that lie within the same order of magnitude as the mean bursting period. The computed first three resonant frequencies at the maximum deformation point of both the rubbers are listed in Table III. It is seen that the first three modal frequencies of both the 60A and 20A implants are of the same order of magnitude as the mean bursting frequency. This overlap in the vibration and bursting frequencies lends credence to the possible interference of the burst cycle by the surface vibrations.

In addition to the turbulent bursts, works since the 2010s have identified that very large-scale motions (VLSMs) within the logarithmic layer of the boundary layer also contributes to a

TABLE III. First three natural frequencies of the rubber implants at maximum deformation points.

Wall type	f_1 (kHz)	f_2 (kHz)	f_3 (kHz)
60A	20.1	41.6	64.4
20A	13.4	28.4	44.9

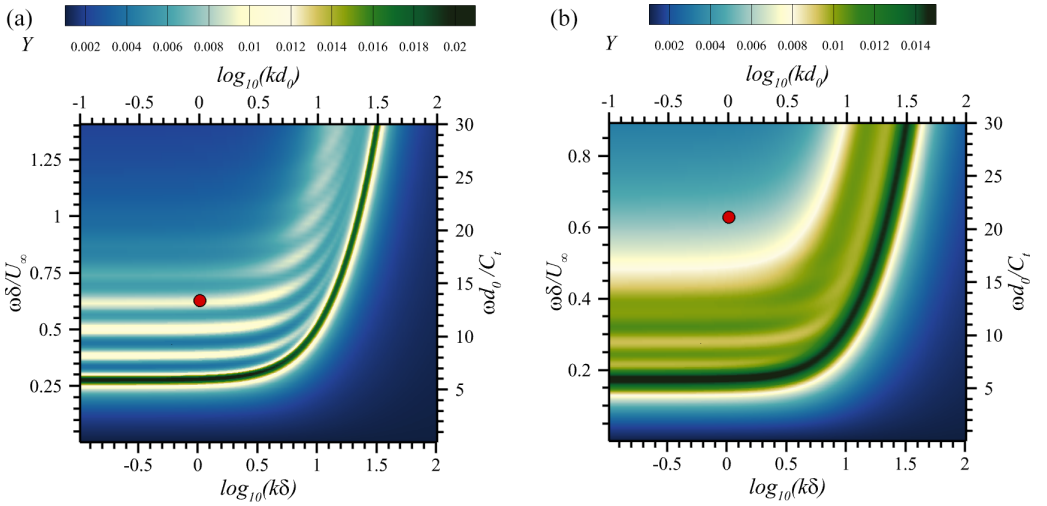

FIG. 9. Calculated admittance spectra for (a) 60A and (b) 20A rubber implants for $k_z = 2\pi/\delta$. The red circle denotes the location of VLSMs in the (k_x, ω) space.

significant fraction of turbulent kinetic energy in the near-wall region and the wall shear stress with increasing Reynolds numbers (Hutchins and Marusic [53]). These large-scale motions have a nonlinear modulating effect on the near-wall small-scale turbulence, which has been quantified in both incompressible and compressible flows by Mathis *et al.* [54] and Pirozzoli and Bernardini [41], respectively. Marusic *et al.* [55] demonstrated that external spanwise wall oscillations at an actuation frequency similar to VLSM (very large-scale motions) frequency can attenuate the large-scale energy, and in turn the skin friction drag. In the case of compliant walls, Luhar *et al.* [45] showed that walls with resonant frequencies that matched the VLSM frequency attenuated the targeted coherent structure, and the associated Reynolds stress. In light of these prior works, we explore the possibility of the surface vibrations impacting the large-scale motions within the boundary layer.

The wavelength and phase speed of the VLSMs are found to be $(\lambda_x, \lambda_z, c) = (6\delta, \delta, 16u_\tau)$ in incompressible flows. Experimental and numerical investigations by Bross *et al.* [56] and Pirozzoli and Bernardini *et al.* [41] found that compressibility effects did not change structural organization of these motions; however, a slight increase in streamwise and spanwise coherence length (10%) was observed. Hence, the incompressible values shall be used for the present study. The viscoelastic equations for the wall were solved numerically in the spectral domain (k_x, ω) for a fixed spanwise wave number of $k_z = 2\pi/\delta$ that corresponds to the spanwise spacing of the VLSMs. Since the spectral information of wall pressure for this spanwise scale is not available, the wall admittance is plotted instead of wall-normal deformation, and is given by

$$Y = \frac{v(k_x, k_z, \omega)}{p(k_x, k_z, \omega)} = -\frac{i\omega s_2(k_x, k_z, \omega)}{p(k_x, k_z, \omega)}. \tag{11}$$

Here v is the wall-normal velocity, s_2 is the wall-normal displacement, and p is the pressure at a particular point in the spectrum. Since the wall deforms linearly, plotting the admittance removes any dependance on the applied forcing and is solely a property of the particular wall being studied. It should be noted that the goal of this analysis is to check the possibility of interactions between the surface and the VLSMs and not to quantify the interaction strength on the flowfield. The spectra of structural admittance of 60A and 20A rubber implants at $k_z = 2\pi/\delta$ is shown in Figs. 9(a) and 9(b). Similar to Fig. 8, both the frequency and streamwise wave number are nondimensionalized in flow and wall relevant scales. The red circle in both Figs. 9(a) and 9(b) denote the spectral

TABLE IV. Wall-normal deformation of viscoelastic surface scaled in inner units.

Wall type	$\zeta^+_{\mathrm{RMS}}\vert_{c=C_t}$	$\zeta^+_{\mathrm{RMS}}\vert_{c=0.7U_\infty}$
60A	0.025	0.006
20A	0.028	0.0148

location of the VLSMs in (k_x, ω) space. It can be observed from Fig. 9 that the admittance spectra of both 60A and 20A rubber implants look very similar qualitatively, except for slightly weaker and diffused resonance peaks for 20A implant case, which is a result of higher material damping. For 60A implant case, it is quite evident that the spectral range of the VLSM structures lie within the envelope of strong material resonances. For the 20A implant case, the VLSMs seem to be slightly offset from the resonant modes; however, energetic scales such as VLSMs span a finite region of wave numbers and frequencies, and hence coupling of similar order may be expected also from the 20A implant. However, it must be noted that the peak admittances (Y) for both Figs. 9(a) and 9(b) are quite small [$\approx O(10^{-2})$], and it is not possible to comment on the strength of these interactions without additional data.

While the frequency overlap with dominant near-wall turbulent structures supports the possibility of favorable interaction and drag reduction, it is also critical to determine if the surface deformation amplitudes are large enough to influence the boundary layer structure and dynamics. To this end, the rms wall-normal deformations were calculated from the deformation spectrum along two phase velocities, $c = C_t$ and $c = 0.7U_\infty$, which correspond to the material shear speed and the convection velocity of pressure fluctuations respectively (Zhang *et al.* [26] and Greidanus *et al.* [28]). Dominant flow structures with similar advection speeds ($0.7U_\infty$) have been consistently observed in the experiments of Zhang *et al.* [26] and Wang *et al.* [27]. The calculated dynamic deformations normalized by the inner length scale $\delta_v (= \nu/u_\tau)$ are presented in Table IV. For a wave speed $c = 0.7U_\infty$, the rms deformations for 60A and 20A are about $0.006\delta_v$ and $0.015\delta_v$, respectively. Evidently, the unsteady deformation amplitudes are much smaller than even the laminar sublayer thickness. However, Wang *et al.* [27] observed that even such unsteady deformation amplitudes are sufficient to the alter the turbulence statistics. In their case, an rms deformation of $0.004\delta_v$ was shown to cause a mean shift of velocity profile in the viscous sublayer, as well as an increased wall-normal and streamwise velocity fluctuations near the wall. A deformation of about $0.06\delta_v$ resulted in downward shift of the log layer, a significant increase in velocity fluctuations, and a mild increase in Reynolds stresses. In the present case, since the unsteady deformation amplitude for 60A rubber implant is about 10 folds smaller than $0.06\delta_v$, no significant changes are expected in the mean and turbulent statistics of the boundary layer; however, the deformation amplitude may be sufficient to cause near-wall burst modulation. For the 20A case, the deformation is about $0.015\delta_v$, which is significant enough to impact the turbulence statistics across the boundary layer, including the burst cycle.

V. CONCLUSIONS

Drag mitigation by disrupting the self-sustaining near-wall cycle has garnered a significant attention over the past several decades, primarily owing to the scalability and practicality of the devices. The present work investigates the application of nonrigid surfaces created by viscoelastic rubber implants, which presents a unique opportunity to engineer the material properties to suit the particular need. Unlike the vast majority of the prior work in this topic that were performed in aqueous medium at incompressible speeds, the present work explores the application of the nonrigid surfaces for skin friction drag mitigation in high-speed air flows. Direct measurements of the skin friction coefficient (C_f) were obtained along the length of two rubber implants of 60A and 20A shore hardnesses and compared against the corresponding values over a rigid surface. Both

rubber implants generated measurable C_f reduction that were above the measurement uncertainty. A maximum local C_f reduction of 30% was obtained with a 20A shore hardness rubber at $x = 80$ mm, which is within 30 mm of the implant leading edge. The C_f over the implants decreased gradually along the streamwise distance, suggesting that the flow response to the presence of the viscoelastic surface is strong at the initial distance from the implant leading edge.

Exploration of the underlying flow or viscoelastic material interactions that caused the observed C_f mitigation was undertaken using a combination of boundary layer measurements and theoretical analysis. The boundary layer thickness and the integral properties was shown to be nearly identical between the rigid plate and rubber implant configurations. The rms turbulent velocity fluctuations and Reynolds stress component $(-u'v')$ in the outer layer of the boundary layer revealed that whereas the streamwise velocity fluctuations over the rubber implants did not measurably differ from the rigid surface, the wall-normal velocity and the Reynolds stress component showed notable differences. Theoretical analysis of the unsteady viscoelastic surface response to the boundary layer pressure fluctuations were made. The unsteady deformation spectrum at $k_z = 0$ and admittance spectrum at $k_z = 2\pi/\delta$ revealed that both the rubber implants assessed exhibit multiple vibration modes whose resonance frequencies overlap with the near-wall turbulent bursting frequencies as well as large-scale motions. The accompanying calculations of the unsteady deformation amplitudes support that the vibration amplitudes of both the implants are potentially sufficient to disrupt or modify the near-wall turbulent activities. Moreover, calculations revealed that both the implants do not undergo any flow-induced structural instabilities. Overall, the measurements and calculations suggest that the potential disruption of the near-wall burst cycles could be one the dominant mechanisms that caused the observed skin friction reduction.

ACKNOWLEDGMENT

The support of the Office of Naval Research (ONR) under Grant No. N00014-21-1-2005 is gratefully acknowledged.

[1] F. M. White, *Fluid Mechanics* (McGraw–Hill, New York, 1966).
[2] H. Schlichting and K. Gersten, *Boundary-Layer Theory* (Springer, Berlin, 2016).
[3] T. C. Corke and F. O. Thomas, Active and passive turbulent boundary-layer drag reduction, AIAA J. **56**, 3835 (2018).
[4] P. Viswanath, Aircraft viscous drag reduction using riblets, Progr. Aerosp. Sci. **38**, 571 (2002).
[5] K.-S. Choi, Near-wall structure of a turbulent boundary layer with riblets, J. Fluid Mech. **208**, 417 (1989).
[6] R. García-Mayoral and J. Jimenez, Hydrodynamic stability and breakdown of the viscous regime over riblets, J. Fluid Mech. **678**, 317 (2011).
[7] H. Choi, P. Moin, and J. Kim, Direct numerical simulation of turbulent flow over riblets, J. Fluid Mech. **255**, 503 (1993).
[8] E. Coustols and J. Cousteix, Performances of riblets in the supersonic regime, AIAA J. **32**, 431 (1994).
[9] L. Gaudet, Properties of riblets at supersonic speed, Appl. Sci. Res. **46**, 245 (1989).
[10] S. K. Robinson, Effects of riblets on turbulence in a supersonic boundary layer (AIAA1988).
[11] L. Duan and M. M. Choudhari, Direct numerical simulations of high-speed turbulent boundary layers over riblets, in *52nd Aerospace Sciences Meeting* (Curran, New York, 2014), p. 0934.
[12] L. Duan and M. Choudhari, Effects of riblets on skin friction and heat transfer in high-speed turbulent boundary layers, in *50th AIAA Aerospace Sciences Meeting Including the New Horizons Forum and Aerospace Exposition* (AIAA Press, Reston, VA, 2012), p. 1108.
[13] W. Breugem, B. Boersma, and R. Uittenbogaard, The influence of wall permeability on turbulent channel flow, J. Fluid Mech. **562**, 35 (2006).

[14] N. Abderrahaman-Elena and R. García-Mayoral, Analysis of anisotropically permeable surfaces for turbulent drag reduction, Phys. Rev. Fluids **2**, 114609 (2017).
[15] G. Gomez-de Segura, A. Sharma, and R. García-Mayoral, Turbulent drag reduction by anisotropic permeable coatings, in *10th International Symposium on Turbulence and Shear Flow Phenomena (TSFP10)* (Chicago, USA, 2017).
[16] Y. Kuwata and K. Suga, Direct numerical simulation of turbulence over anisotropic porous media, J. Fluid Mech. **831**, 41 (2017).
[17] M. E. Rosti, L. Brandt, and A. Pinelli, Turbulent channel flow over an anisotropic porous wall–drag increase and reduction, J. Fluid Mech. **842**, 381 (2018).
[18] M. T. Landahl, On the stability of a laminar incompressible boundary layer over a flexible surface, J. Fluid Mech. **13**, 609 (1962).
[19] P. Carpenter and A. Garrad, The hydrodynamic stability of flow over kramer-type compliant surfaces. Part 1. Tollmien-schlichting instabilities, J. Fluid Mech. **155**, 465 (1985).
[20] P. Carpenter and A. Garrad, The hydrodynamic stability of flow over kramer-type compliant surfaces. Part 2. Flow-induced surface instabilities, J. Fluid Mech. **170**, 199 (1986).
[21] J. H. Duncan, The response of an incompressible, viscoelastic coating to pressure fluctuations in a turbulent boundary layer, J. Fluid Mech. **171**, 339 (1986).
[22] T. Lee, M. Fisher, and W. Schwarz, Investigation of the stable interaction of a passive compliant surface with a turbulent boundary layer, J. Fluid Mech. **257**, 373 (1993).
[23] K.-S. Choi, X. Yang, B. Clayton, E. Glover, M. Atlar, B. Semenov, and V. Kulik, Turbulent drag reduction using compliant surfaces, Proc. R. Soc. Lond. A **453**, 2229 (1997).
[24] S. Xu, D. Rempfer, and J. Lumley, Turbulence over a compliant surface: Numerical simulation and analysis, J. Fluid Mech. **478**, 11 (2003).
[25] E. Kim and H. Choi, Space–time characteristics of a compliant wall in a turbulent channel flow, J. Fluid Mech. **756**, 30 (2014).
[26] C. Zhang, J. Wang, W. Blake, and J. Katz, Deformation of a compliant wall in a turbulent channel flow, J. Fluid Mech. **823**, 345 (2017).
[27] J. Wang, S. S. Koley, and J. Katz, On the interaction of a compliant wall with a turbulent boundary layer, J. Fluid Mech. **899**, A20 (2020).
[28] A. Greidanus, R. Delfos, S. Picken, and J. Westerweel, Response regimes in the fluid–structure interaction of wall turbulence over a compliant coating, J. Fluid Mech. **952**, A1 (2022).
[29] M. E. Rosti and L. Brandt, Numerical simulation of turbulent channel flow over a viscous hyper-elastic wall, J. Fluid Mech. **830**, 708 (2017).
[30] H. T. Pham, Z. N. Gianikos, and V. Narayanaswamy, Compression ramp induced shock-wave/turbulent boundary-layer interactions on a compliant material, AIAA J. **56**, 2925 (2018).
[31] J. Walz and V. Narayanaswamy, Dual separation control and drag mitigation in high speed flows using viscoelastic materials, Phys. Fluids **35**, 031704 (2023).
[32] J. D. Pickles, B. R. Mettu, P. K. Subbareddy, and V. Narayanaswamy, Sharp-fin induced shock wave/turbulent boundary layer interactions in an axisymmetric configuration, in *47th AIAA Fluid Dynamics Conference* (AIAA Press, Reston, VA, 2017).
[33] J. D. Pickles, B. R. Mettu, P. K. Subbareddy, and V. Narayanaswamy, Gas density field imaging in shock dominated flows using planar laser scattering, Exp. Fluids **59**, 112 (2018).
[34] J. D. Pickles, B. R. Mettu, P. K. Subbareddy, and V. Narayanaswamy, On the mean structure of sharp-fin-induced shock wave/turbulent boundary layer interactions over a cylindrical surface, J. Fluid Mech. **865**, 212 (2019).
[35] M. L. Funderburk and V. Narayanaswamy, Investigation of negative surface curvature effects in axisymmetric shock/boundary-layer interaction, AIAA J. **57**, 1594 (2019).
[36] J. W. Naughton and M. Sheplak, Modern developments in shear-stress measurement, Prog. Aeronaut. Sci. **38**, 515 (2002).
[37] E. Schülein, Skin friction and heat flux measurements in shock/boundary layer interaction flows, AIAA J. **44**, 1732 (2006).

[38] J. Hubner and B. Carroll, Thin-oil-film interferometric skin-friction measurements in short-duration supersonic flow, Exp. Fluids **15-15**, 315 (1993).
[39] J. Naughton and M. Hind, Multi-image oil-film interferometry skin friction measurements, Meas. Sci. Technol. **24**, 124003 (2013).
[40] M. B. Priestley, *Spectral Analysis and Time Series* (Academic Press, London, 1981), Vol. 890.
[41] S. Pirozzoli and M. Bernardini, Turbulence in supersonic boundary layers at moderate Reynolds number, J. Fluid Mech. **688**, 120 (2011).
[42] D. Coles, The law of the wake in the turbulent boundary layer, J. Fluid Mech. **1**, 191 (1956).
[43] Y. Hou, *Particle Image Velocimetry Study of Shock-induced Turbulent Boundary Layer Separation*, Ph.D. thesis (The University of Texas at Austin, 2003).
[44] M. Elena and J.-P. Lacharme, Experimental study of a supersonic turbulent boundary layer using a laser doppler anemometer, J. Mec. Theor. Appl. **7**, 175 (1988).
[45] M. Luhar, A. S. Sharma, and B. McKeon, A framework for studying the effect of compliant surfaces on wall turbulence, J. Fluid Mech. **768**, 415 (2015).
[46] M. Gad-El-Hak, R. F. Blackwelder, and J. J. Riley, On the interaction of compliant coatings with boundary-layer flows, J. Fluid Mech. **140**, 257 (1984).
[47] M. Gad-el Hak, The response of elastic and viscoelastic surfaces to aturbulent boundary layer, J. Appl. Mech., **53**, 206 (1986).
[48] R. Hansen and D. Hunston, An experimental study of turbulent flows over compliant surfaces, J. Sound Vib. **34**, 297 (1974).
[49] L. D. Landau, E. M. Lifshitz, A. M. Kosevich, and L. P. Pitaevskii, *Theory of Elasticity* (Elsevier, Amsterdam 1986), Vol. 7.
[50] M. Goody, Empirical spectral model of surface pressure fluctuations, AIAA J. **42**, 1788 (2004).
[51] S. J. Beresh, J. F. Henfling, R. W. Spillers, and B. O. Pruett, Fluctuating wall pressures measured beneath a supersonic turbulent boundary layer, Phys. Fluids **23**, 075110 (2011).
[52] R. Blackwelder and J. Haritonidis, Scaling of the bursting frequency in turbulent boundary layers, J. Fluid Mech. **132**, 87 (1983).
[53] N. Hutchins and I. Marusic, Large-scale influences in near-wall turbulence, Philos. Trans. R. Soc. A **365**, 647 (2007).
[54] R. Mathis, N. Hutchins, and I. Marusic, Large-scale amplitude modulation of the small-scale structures in turbulent boundary layers, J. Fluid Mech. **628**, 311 (2009).
[55] I. Marusic, D. Chandran, A. Rouhi, M. K. Fu, D. Wine, B. Holloway, D. Chung, and A. J. Smits, An energy-efficient pathway to turbulent drag reduction, Nat. Commun. **12**, 5805 (2021).
[56] M. Bross, S. Scharnowski, and C. J. Kähler, Large-scale coherent structures in compressible turbulent boundary layers, J. Fluid Mech. **911**, A2 (2021).